AGU PUBLICATIONS

JGR

Journal of Geophysical Research: Biogeosciences

RESEARCH ARTICLE
10.1002/2014JG002754

Key Points:
- Landsat direct, diffuse, and total FPARs estimation
- Field direct and diffuse FPAR estimation
- Differences between FPAR definitions and influences on APAR

Correspondence to:
W. Li,
wenjuan.li122@gmail.com

Citation:
Li, W., and H. Fang (2015), Estimation of direct, diffuse, and total FPARs from Landsat surface reflectance data and ground-based estimates over six FLUXNET sites, *J. Geophys. Res. Biogeosci.*, *120*, 96–112, doi:10.1002/2014JG002754.

Received 28 JUL 2014
Accepted 13 DEC 2014
Accepted article online 18 DEC 2014
Published online 22 JAN 2015

Estimation of direct, diffuse, and total FPARs from Landsat surface reflectance data and ground-based estimates over six FLUXNET sites

Wenjuan Li[1,2] and Hongliang Fang[1]

[1]LREIS, Institute of Geographic Sciences and Natural Resources Research, Chinese Academy of Sciences, Beijing, China, [2]University of Chinese Academy of Sciences, Beijing, China

Abstract The fraction of photosynthetically active radiation (PAR) absorbed by green elements (FPAR) is an essential climate variable in quantifying canopy absorbed PAR (APAR) and gross and net primary production. Current satellite FPAR products typically correspond to black-sky FPAR under direct illumination only, but the radiation transfer and vegetation absorption processes differ for direct and diffuse PARs. To address this, the present study developed a new approach to estimate direct, diffuse, and total FPARs, separately, from Landsat surface reflectance data. Field-measured direct and diffuse FPARs were first derived for crops, deciduous broadleaf forests, and evergreen needleleaf forests at six FLUXNET sites. Then, a coupled soil-leaf-canopy radiative transfer model (SLC) was used to simulate surface reflectance under direct and diffuse illumination conditions. Direct, diffuse, and total FPARs were estimated by comparing Landsat-5 Thematic Mapper (TM) data and simulated surface reflectances using a lookup table approach. The differences between the Landsat-estimated and the field-measured FPARs are less than 0.05 (10%). The diffuse FPAR is higher than the direct FPAR by up to 19.38%, whereas the total FPAR is larger than the direct FPAR by up to 16.07%. The direct APAR is higher than the diffuse APAR under clear-sky conditions, but underestimates the total APAR by $-277.72\ \mu mol\ s^{-1}\ m^{-2}$ on average. The approach described here can be extended to estimate direct, diffuse, and total FPARs from other satellite data and the obtained FPAR variables could be helpful to improve modeling of vegetation processes.

1. Introduction

The fraction of photosynthetically active radiation (PAR) absorbed by green elements (FPAR) can be defined as the ratio of total absorbed PAR (APAR) to incoming PAR at the top of the canopy and represents the energy absorption efficiency of the canopy for downwelling PAR. Specified as an essential climate variable by the Global Climate Observing System [*Global Climate Observing System*, 2011], FPAR is a critical parameter in characterizing energy, mass, and momentum exchanges between the canopy and the atmosphere and is required for photosynthesis and primary production simulations [*Gobron and Verstraete*, 2009].

FPAR represents the summed canopy absorption efficiency for both direct and diffuse PAR. It has been demonstrated that FPAR is larger under totally diffuse than clear-sky conditions because all canopy parts can absorb lights effectively under diffuse conditions, whereas some portions of the canopy will be shaded under direct light conditions [*Goward and Huemmrich*, 1992; *Nouvellon et al.,* 2000; *Thomas et al.,* 2006]. Therefore, the direct and diffuse FPARs are commonly defined, separately, as the FPAR values obtained under clear (most sunny) and overcast (most cloudy) conditions, respectively [*Thomas et al.,* 2006].

In the field, direct and diffuse FPARs can be calculated from the transmitted and reflected PARs measured separately under direct and diffuse illumination conditions [*Gobron et al.,* 2006]. However, field measurements are usually difficult to obtain under variable sky conditions [*Gu et al.,* 2002]. Direct and diffuse FPARs have also been estimated as a function of leaf area index (LAI), leaf transmission, or scattering coefficients in land surface models, such as the Common Land Model [*Dai et al.,* 2003], Basin Irrigation System [*Foley et al.,* 1996], and Simple Biosphere 2 [*Sellers*, 1985]. However, several studies have reported that both direct and diffuse FPARs are underestimated in current land surface models because of the simplification of radiative transfer processes [*Senna et al.,* 2005; *Tian et al.,* 2004].

Satellite FPAR products have been generated at different temporal and spatial resolutions, such as Moderate Resolution Imaging Spectroradiometer (MODIS) [*Knyazikhin et al.,* 1998], VGT bioGEOphysical product Version 1(GEOV1) [*Baret et al.,* 2013], Medium-Resolution Imaging Spectrometer (MERIS) [*Gobron et al.,* 1999], and Joint Research Centre Two-stream Inversion Procedure (JRC-TIP) [*Pinty et al.,* 2011]. MODIS FPAR product is derived from the inversion of biome-based 3-D radiative transfer model using the lookup table approach. The GEOV1 product is generated from neural networks trained by using the "best estimates" of FPAR obtained by fusion of MODIS and CYCLOPES FPAR products. The MERIS FPAR product is computed as a function of rectified red and near-infrared (NIR) bands reflectance and several polynomial coefficients which are optimized using a training dataset generated from a 1-D semidiscrete land-surface-atmosphere coupled RT model. The JRC-TIP FPAR product is derived based on MODIS broadband visible and NIR albedo (black-sky and white-sky) products from combined Terra-Aqua data sets. The MODIS, GEOV1, and MERIS FPAR products are retrieved as the instantaneous black-sky FPAR under direct illumination, without considering the relative proportion of diffuse radiation in the total radiation. However, even under fully clear-sky conditions, the proportion of diffuse PAR over the surface cannot be ignored [*Gu et al.,* 2002]. Otherwise, FPAR will be underestimated, especially for small leaf area index (LAI) region [*Goward and Huemmrich*, 1992; *Tian et al.,* 2004]. The JRC-TIP algorithm generates direct FPAR and diffuse FPARs, separately, but the product has not been fully validated due to the lack of companion field measurements.

The present study aims to estimate direct, diffuse, and total FPARs from Landsat reflectance data. The advantages of the high-resolution (30 m) Landsat data make them appealing for local photosynthesis and primary production studies and for the validation of current moderate-resolution FPAR products. In this study, a coupled soil-leaf-canopy (SLC) radiative transfer model [*Verhoef and Bach*, 2007] was used to estimate direct and diffuse FPARs from 30 m Landsat surface reflectance data. Six FLUXNET sites including crops, deciduous broadleaf forests, and evergreen needleleaf forests were selected to derive field direct and diffuse FPARs and to validate the Landsat estimates. Here the total and direct FPARs are compared and the influences of different FPAR components on APAR estimation are explored. The results of this study will be invaluable for the generation of FPAR products and future studies utilizing regional and global direct, diffuse, and total FPAR products.

2. Methods and Measurements

2.1. Theory

The instantaneous total APAR at the top of the canopy (TOC) is a sum of the direct and diffuse APARs.

$$\mathrm{APAR}_t(\theta_s) = \mathrm{APAR}_{\mathrm{dir}}(\theta_s) + \mathrm{APAR}_{\mathrm{dif}}(\theta_s) \tag{1}$$

where APAR_t, $\mathrm{APAR}_{\mathrm{dir}}$, and $\mathrm{APAR}_{\mathrm{dif}}$ represent total APAR, direct APAR, and diffuse APAR at solar zenith angle θ_s, respectively.

$$\mathrm{APAR}_{\mathrm{dir}}(\theta_s) = \mathrm{PAR}_{\mathrm{dir}}(\theta_s) \times \mathrm{FPAR}_{\mathrm{dir}}(\theta_s) \tag{2}$$

$$\mathrm{APAR}_{\mathrm{dif}}(\theta_s) = \mathrm{PAR}_{\mathrm{dif}}(\theta_s) \times \mathrm{FPAR}_{\mathrm{dif}} \tag{3}$$

where $\mathrm{PAR}_{\mathrm{dir}}$, $\mathrm{FPAR}_{\mathrm{dir}}$, $\mathrm{PAR}_{\mathrm{dif}}$, and $\mathrm{FPAR}_{\mathrm{dif}}$ represent instantaneous direct PAR, direct FPAR, diffuse PAR, and diffuse FPAR, respectively. Direct and diffuse FPAR corresponds to the canopy absorption capacity for direct and diffuse incoming PAR, respectively. Note that diffuse FPAR is invariant with the solar zenith angle (SZA) (section 3.1).

By substituting equations (2) and (3) into equation (1), and dividing by total PAR on both sides, the total FPAR at the top of the canopy (TOC) can be expressed as a weighted sum of direct and diffuse FPARs, as follows:

$$\mathrm{FPAR}_{\mathrm{tol}}(\theta_s) = (1 - \mathrm{skyl}(\theta_s)) \cdot \mathrm{FPAR}_{\mathrm{dir}}(\theta_s) + \mathrm{skyl} \cdot \mathrm{FPAR}_{\mathrm{dif}} \tag{4}$$

where $\mathrm{FPAR}_{\mathrm{tol}}$ and skyl represent total FPAR and the instantaneous proportion of diffuse PAR in the total incoming PAR, respectively.

According to equation (4), the instantaneous direct FPAR can be calculated if the total FPAR, diffuse ratio and diffuse FPAR are known

$$\mathrm{FPAR}_{\mathrm{dir}}(\theta_s) = (\mathrm{FPAR}_{\mathrm{tol}}(\theta_s) - \mathrm{skyl} \cdot \mathrm{FPAR}_{\mathrm{dif}}) / (1 - \mathrm{skyl}(\theta_s)) \tag{5}$$

Journal of Geophysical Research: Biogeosciences 10.1002/2014JG002754

Table 1. Six FLUXNET Sites and the Available Landsat Scenes[a]

Station Name	Country	Location	Surface Type	Canopy Height	Sensors Height	Period	Landsat Path/Row	Scene Time	References
Mead Irrigated (Mead NE1)	USA	41.17° N, 96.48° W	Continuous maize	3.5 m	TOC: 5.5 m (↓), 5.5 m (↑) BOC: ground (↓↑)	2003.1 to 2010.10	28/31	May–September	*Verma et al.* [2005]
Mead Irrigated Rotation (Mead NE2)	USA	41.17° N, 96.47° W	Maize-soybean	3.4 m (maize) 1 m (soybean)	TOC: 5.5 m (↓), 5.5 m (↑) BOC: ground (↓↑)	2003.1 to 2010.10	28/31	May–September	*Verma et al.* [2005]
Mead Rainfed (Mead NE3)	USA	41.18° N, 96.44° W	Maize-soybean	2.7 m (maize) 0.8 m (soybean)	TOC: 5.5 m (↓), 5.5 m (↑) BOC: ground (↓↑)	2003.1 to 2010.12	28/31	May–September	*Verma et al.* [2005]
Bartlett Experimental Forest (Bartlett)	USA	44.07° N, 71.29° W	Deciduous broadleaf forest	19 m	TOC: 25 m (↓), 23.8 m (↑), BOC: 1 m (↓)	2004.7 to 2007.9	13/29	April–September	*Jenkins et al.* [2007] *Ollinger and Smith* [2005]
Soroe	Denmark	55.49° N, 11.65° E	Deciduous broadleaf forest	30 m	TOC: 57 m (↓), 53.5 m (↑), BOC:*	2006.9 to 2010.10	195/21	April–September	*Pilegaard et al.* [2001]
Tharandt	Germany	50.96° N, 13.57° E	Evergreen needleleaf forest	30 m	TOC: 37 m (↓), 37 m (↑), BOC: 17 m (↓)	2004.8 to 2010.10	192/25	January–December	*Grumwald and Bernhofer* [2007]

[a]Canopy height represents the height at peak stage, and sensor height is the distance between sensor and ground. Downward (↓) and upward (↑) arrows indicate downwelling radiation and upwelling radiation measurements. TOC: the top of canopy; BOC: bottom of canopy. The information about the below-canopy PAR sensors used to measure the soil reflected PAR is from personal contact with the PI. The time of Landsat scenes was determined from the field measurements.

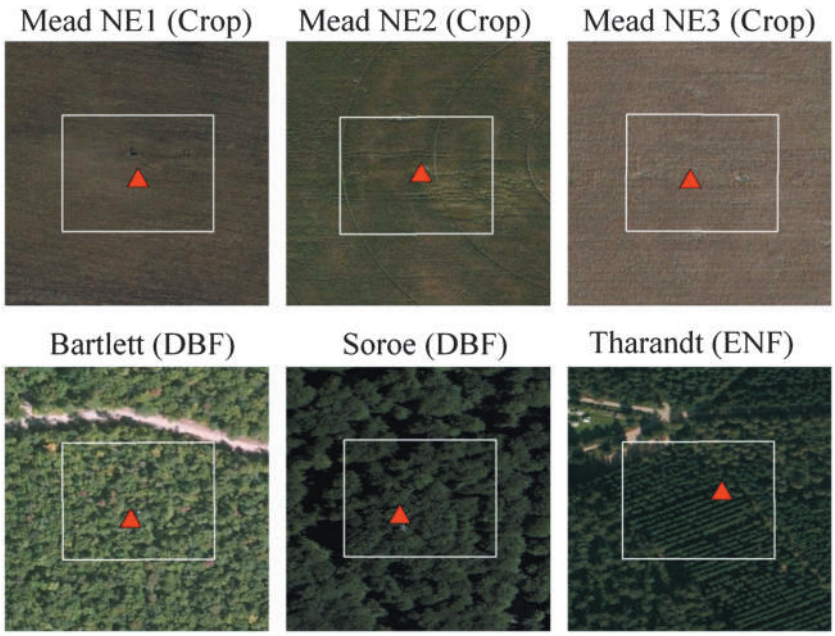

Figure 1. High-resolution images of six flux sites acquired from map.bing.com/maps in spatial scale of 1:1500. White squares represent the 3 × 3 Landsat pixels (90 × 90 m), with central pixel covering each tower (red rectangles). DBF: deciduous broadleaf forest; ENF: evergreen needleleaf forest.

2.2. Estimation of FPARs From Field Measurements

2.2.1. Site Descriptions

Six sites from the FLUXNET project (http://public.ornl.gov/FLUXNET/), covering crops, deciduous broadleaf forests (DBF), and evergreen needleleaf forests (ENF) were assembled for this study (Table 1). The selection of sites was based on spatial homogeneity, the representativeness of each vegetation type, and the available PAR measurements (total downwelling PAR, diffuse PAR, above-canopy reflected PAR, below-canopy transmitted PAR, and the soil reflected PAR). Since the field measurements were to be compared with the satellite-derived variables, each site had to be spatially homogeneous around the tower. Figure 1 shows the area and dominant vegetation type for a 90 m × 90 m area (3 by 3 Landsat pixels) centered on each tower.

All selected sites are equipped with two PAR sensors above the canopy, with one pointing toward the sky to measure the incoming total PAR, and the other facing downward to measure the surface reflected PAR. At each site, a sunshine sensor is mounted above the canopy to measure the total downwelling and diffuse component of the downwelling PAR. Direct PAR can be calculated from the differences between total and diffuse PAR. Three crop sites, Mead NE1, NE2, and NE3, are equipped with downward looking PAR sensors below the canopy to measure the reflected background PAR. For forest sites, the background albedo was ignored because most of the Landsat scenes were acquired during the growing season when the background albedo was negligibly small [*D'Odorico et al.,* 2014; *Jenkins et al.,* 2007; *Nouvellon et al.,* 2000]. Five upward looking PAR sensors at the three Mead sites and six at the Bartlett site [*Jenkins et al.,* 2007] are installed below the canopy to measure the transmitted PAR. At the other sites, one upward PAR sensor is used to measure the transmitted PAR.

As FPAR varies with the solar zenith angle, the instantaneous FPAR close to the satellite overpass time (10:00 A.M. for Landsat thematic mapper (TM) was extracted. At the Mead sites, field FPAR measurements are obtained every hour. For the present study, the instantaneous FPAR value was calculated by averaging FPAR from 9:30 A.M. to 10:30 A.M. At all forest sites, field measurements are typically made every half hour; here, the FPAR data at 10:00 am were selected for comparison with Landsat estimates. The instantaneous diffuse ratio was calculated as the ratio of the diffuse PAR to the total PAR.

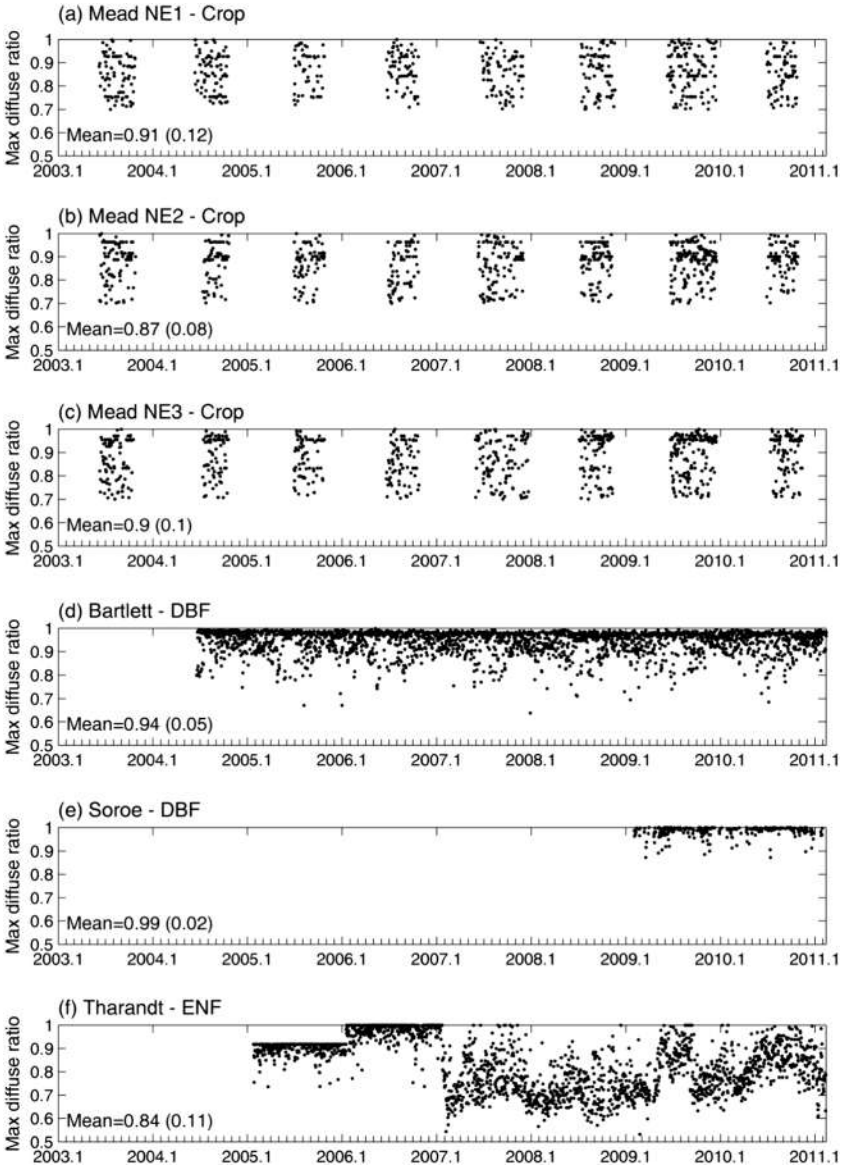

Figure 2. Seasonal variation of daily maximum diffuse ratio from field measurements at six sites, (a) Mead NE1, (b) Mead NE2, (c) Mead NE3, (d) Bartlett, (e) Soroe, and (f) Tharandt. The mean maximum diffuse ratio (and the standard deviation) is also shown in the lower left corner.

2.2.2. Estimation of Field FPARs

The instantaneous total FPAR can be estimated from the PAR measurements described above, as follows [*Goward and Huemmrich*, 1992]:

$$\mathrm{FPAR_{tol}} = \frac{\mathrm{PAR}_i - \mathrm{PAR}_r - (\mathrm{PAR}_t - \mathrm{PAR}_s)}{\mathrm{PAR}_i} \tag{6}$$

where PAR_i is the total incoming PAR at TOC, PAR_r is the canopy reflected PAR, PAR_t is the canopy transmitted PAR, and PAR_s is the PAR reflected from the soil surface. The term in parenthesis represent the PAR absorbed by the soil. At the three forest sites, PAR_s is ignored.

When the canopy remains stable (no sudden changes), the diffuse FPAR can be considered as an intrinsic attribute of the canopy and is independent of atmospheric conditions and solar zenith angles. In this case,

Table 2. List of Variables Required to Run SLC Model and Their Ranges

	Variables	Description	Unit	Ranges or Values
Geometric configuration	θ_v	View zenith angle	°	0
	θ_s	Solar zenith angle	°	0 5 10 15 20 25 30 35 45 50 55 60
	θ_z	Relative azimuth angle	°	90
Canopy structure	LAI	Leaf area index		0–15.0
	$LIDF_a$	LIDF parameter a, controls the average leaf slope		−0.35
	$LIDF_b$	LIDF parameter b, controls the distribution's bimodality		−0.15
	S_l	Hot spot parameter		0.1–0.5
	fb	Fraction of brown components		0 (crops)0–0.5 (forests)
	D	Layer dissociation factor		0–0.5
	C_v	Crown cover		0.6–1.0
	zeta	Crown diameter/crown height		0.5–1.0
Leaf optical properties of green layer	C_{ab}	Leaf chlorophyll a + b content	$\mu g\ cm^{-2}$	20–90
	C_w	Relative water		0.6–0.85
	C_{dm}	Leaf dry matter content	$g\ cm^{-2}$	0.003–0.01
	C_s	Leaf brown pigment		0
	N	Leaf mesophyll structure		1.2–2.2
Leaf optical properties of brown layer	C_{ab}	Leaf chlorophyll a + b content	$\mu g\ cm^{-2}$	0
	C_w	Relative water		0.6–0.85
	C_{dm}	Leaf dry matter content	$g\ cm^{-2}$	0.003–0.01
	C_s	Leaf brown pigment		0.1–3.5
	N	Leaf mesophyll structure		1.2–2.2
Soil	soil_b	Soil brightness		0.5–1.0

the total FPAR measured with the largest diffuse ratio (close to 1.0) can be approximated as the diffuse FPAR. Based on the instantaneous diffuse ratio at 10:00 A.M., the sky conditions are divided into clear (diffuse ratio < 0.2), partly clear (diffuse ratio $0.2 \sim 0.8$), and overcast (diffuse ratio > 0.8) conditions. The overcast sky was excluded from the direct FPAR calculation. For clear and partly clear-sky conditions, the instantaneous diffuse ratio during a day was calculated and the diffuse FPAR was determined based on three criteria: (1) the instantaneous diffuse ratio was the largest; (2) the next diffuse ratio measurement should also be large in case of sudden clouds; (3) the incoming PAR measurement is larger than 10.0 $\mu mol\ s^{-1}\ m^{-2}$ and the calculated total FPAR is within 0 to 1.0. The daily maximum diffuse ratio satisfying these criteria along the year was shown in Figure 2. The instantaneous total FPAR measured with the maximum diffuse ratio was treated as a proxy of the diffuse FPAR, and the direct FPAR in the morning was estimated from the diffuse FPAR, the total FPAR, and diffuse ratio at the same time (equation (5)). Besides, the daily instantaneous direct and diffuse APARs at 10:00 A.M. were also calculated from the corresponding PAR and FPAR (equations (2) and (3)). Note that the FPARs measured in these sites include the contributions from all components of the canopy (green leaves, yellow leaves, branches, trunks, and seeds). The rainy days (precipitation > 0) were excluded from the analysis because of the large deviations in the field measurements.

2.3. Estimation of FPARs From Landsat

2.3.1. SLC Model and Simulation

A hybrid soil-leaf-canopy (SLC) model [*Verhoef and Bach*, 2007] was used in this study. The model couples the 4SAIL2 canopy reflectance model, the PROSPECT leaf optical model [*Jacquemoud and Baret*, 1990] and 4SOIL soil reflectance model. 4SAIL2 model is a revised version of the SAIL model [*Verhoef*, 1984]. It separates the canopy into green and brown components by using the fraction brown elements (fb) and the dissociation factor (D), which determines the distribution of the two layers. If the brown leaves are homogeneously distributed, the D value equals to 0; and if all the brown elements are at the bottom of the canopy, the D value equals to 1.0 [*Laurent et al.,* 2011a]. The 4SAIL2 model also includes the crown clumping effect through the crown cover (C_v) and the shape factor (zeta), calculated as the ratio of the crown diameter to the height of

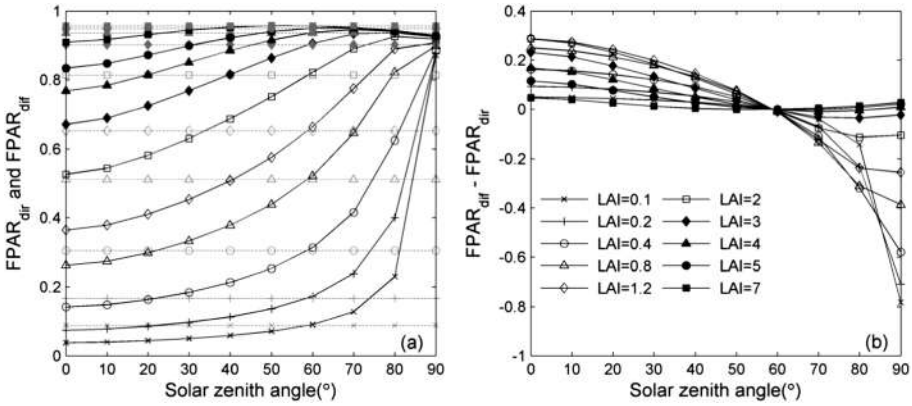

Figure 3. Characteristics of diffuse and direct FPARs under different SAZ and LAI values simulated with SLC model. (a) Diffuse ($FPAR_{dif}$) (gray dashed line) and direct FPAR ($FPAR_{dir}$) (black solid line) variations and (b) the difference between diffuse and direct FPAR, as a function of solar zenith angle and LAI. SLC model parameters: $\theta_v = 0°$, $\theta_z = 90°$, $LIDF_a = -0.35$, $LIDF_b = -0.15$, $S_l = 0.05$, $fb = 0$, $D = 0$, $C_v = 1$, $zeta = 0.2$, $C_{ab} = 60$, $C_w = 0.005$, $C_{dm} = 0.002$, $C_s = 0.03$, $N = 2$, and soil_$b = 0.5$.

the crown center above ground. To simulate the optical properties of green and brown elements, the PROPECT model [*Jacquemoud and Baret*, 1990] includes the concentration in brown material (C_s) [*Verhoef and Bach*, 2003] was used. The leaf optical model was run twice for the green layer and brown layer separately if the fb value is larger than 0. The soil bidirectional reflectance distribution function (BRDF) model 4SOIL was used in SLC, which is an extended version of the Hapke model [*Laurent et al.,* 2011a] that includes hotspot and soil moisture effect.

Table 2 lists the input SLC parameters and their values. The view zenith angle was set as nadir due to the small BRDF effect within a single Landsat scene [*Meroni et al.,* 2013]. To avoid too wide input parameters, the spherical leaf inclination distribution function ($LIDF_a = -0.35$, $LIDF_b = -0.15$) was considered. The fraction brown component (fb) was fixed to 0 for crops, as only the greenup to senescence stages maturation stages were simulated. The fb varies between 0 and 0.5 for forests to take into account the impact of nongreen vegetation (barks, tree trunk, etc.) [*Laurent et al.,* 2011b]. The *D* value was varying from 0 to 0.5 to simulate the distribution of green and brown elements in a canopy. The values of other input parameters were selected in agreement with the literatures [*Baret et al.,* 2007; *Laurent et al.,* 2011b; *Laurent et al.,* 2013; *Verhoef and Bach*, 2007; *Zhang et al.,* 2005].

2.3.2. Landsat Surface Reflectance Data

The Landsat-5 TM surface reflectance products are available through the U.S. Geological Survey Landsat Surface Reflectance Climate Data Record web portal (http://landsat.usgs.gov/CDR_LSR.php). The reflectance product is derived from standard L1t files using the Landsat Ecosystem Disturbance Adaptive Processing System at the NASA Goddard Space Flight Center [*Masek et al.,* 2006]. This product has been validated over several sites and proven to perform successfully over vegetated areas with no adjacent water [*Maiersperger et al.,* 2013]. The reflectance product has been used as an input for deriving global LAI [*Ganguly et al.,* 2012], albedo [*Shuai et al.,* 2011], and crop gross primary production [*Gitelson et al.,* 2012].

A total of 119 Landsat TM scenes without visual cloud and cloud shadow contamination over the study area were selected to derive direct, diffuse, and total FPARs (Table 1). For the crop and DBF sites, images from greenup to senescence stages were used, while all yearlong images were used for the ENF site. For each scene, a 3×3 grid area (90×90 m) centered on the pixel covering the observation tower was extracted to represent the average status of each site. The green, red, and NIR bands were used because they are highly responsive to leaf pigment content, canopy architecture, and leaf structure [*Houborg et al.,* 2009].

2.3.3. The Lookup Table Approach

A widely used lookup table (LUT) approach was selected to invert direct and diffuse FPARs as it could find the global minimum of the cost function. The LUT was generated by running the SLC model in the forward mode with the input variables listed in Table 2. Two separate LUT databases were generated for forests and non-forests sites with different brown pigment fraction values (Table 2). For each SZA, 500,000 randomly

distributed cases were simulated for different variable combinations. The top of canopy reflectance was simulated for each wavelength, and then integrated into the Landsat 5 bands. The final LUT databases used for inversion contain SZA, LAI, the simulated direct and diffuse FPARs, and the simulated surface reflectance in the nadir direction on each Landsat 5 band.

In the actual inversion, the measured Landsat surface reflectance on green, red, and NIR bands, and geometric configuration of each observation (SZA) are required. The nearest simulated geometric configuration was first determined by comparing the simulated and real SZA values. Under this geometric condition, a cost function was established to minimize the differences between simulated and measured surface reflectance for all bands by calculating the relative root-mean-square error (RRMSE) [*Weiss et al.,* 2000]:

$$\mathrm{RRMSE} = \sqrt{\frac{1}{N}\cdot\sum_{i=1}^{N}\left(\frac{\rho_i^{\mathrm{mea}}-\rho_i^{\mathrm{sim}}}{\rho_i^{\mathrm{mea}}}\right)^2} \tag{7}$$

where N is the total number of bands used in the inversion, and ρ_i^{mea} and ρ_i^{sim} are the simulated and satellite-estimated surface reflectances, respectively, for band i.

The RRMSE values were sorted, the first 100 records with the smallest RRMSE were selected and averaged for each pixel [*Darvishzadeh et al.,* 2008]. Site level results were calculated by averaging all pixels within the site. The $\mathrm{FPAR}_{\mathrm{tol}}$ value was calculated from equation (4), using the field-measured diffuse ratio.

3. Results

3.1. The Simulated Direct and Diffuse FPARs

Figure 3 illustrates the relationship between the simulated direct and diffuse FPARs and SZA and LAI. At a given solar zenith angle, both direct and diffuse FPARs increase with LAI. When the solar zenith angle is zero, the direct and diffuse FPARs increase from 0.04 to 0.84 when LAI is less than 2.0. Moreover, these FPARs are nearly saturated ($>$0.9) and increase slightly ($-$0.01) when LAI is larger than 4.0.

The relationship between direct FPAR and SZA is influenced by the LAI value (Figure 3a). At low and intermediate LAIs (LAI $<$ 4), the direct FPAR increases substantially with SZA. And the change rate of direct FPAR with SZA increases with LAI. This can be explained by the longer path of direct radiation penetrating the canopy at higher SZA. When LAI is greater than 4.0, the change rate of direct FPAR with SZA remains invariant for SZA from 0° to 70° and decreases slightly ($-$0.04) for large SZA near the horizon, which can be attributed to FPAR saturation at large LAI. In contrast, for a given LAI, the diffuse FPAR remains invariant for varying SZA values.

The differences between the direct and diffuse FPARs also vary with SZA and LAI (Figure 3b). For canopies with small and intermediate LAIs (LAI $<$ 4), the diffuse FPAR is systematically larger than the direct FPAR (0.02–0.3) when the SZA is smaller than 60°. In contrast, for larger SZA (SZA $>$ 60°), the direct FPAR increases greatly, and the diffuse FPAR is smaller than the direct FPAR ($-0.8 \sim -0.15$). The long penetrating path resulting from large SZA increases the efficiency of a small canopy in absorbing direct PAR. But for canopy with LAI greater than 4, the diffuse FPAR is slightly larger than the direct FPAR for all solar zenith angles.

3.2. The Field FPARs

3.2.1. Seasonal Variation of Field-Measured FPARs

The field FPARs from three crop sites and two DBF sites exhibit a clear seasonal variation (Figure 4). The crop FPAR values increase around the end of May or early June, reach maximum in August and September, and begin to decrease around October. The small phonological variation (e.g., Figure 4c) in different years is mainly due to the plant rotation between maize and soybean [*Verma et al.,* 2005]. At the Bartlett site, the FPARs start to increase in April, reach the peak during June to September, and begin to decrease in early October. The lowest total FPAR of nearly 0.3 can be obtained in the winter season. The FPARs in the Soroe site follow a similar seasonal cycle, with the highest total FPAR (0.98) in July to September and the lowest value (around 0.4) in winter season. The FPARs at the ENF site show little variation throughout the year.

At all sites, the diffuse FPAR is consistently higher than the direct FPAR by 0.02–0.06 (2.53–8.56%) before the senescent (Figure 4 and Table 3), indicating that the green canopy generally absorbs the diffuse PAR more

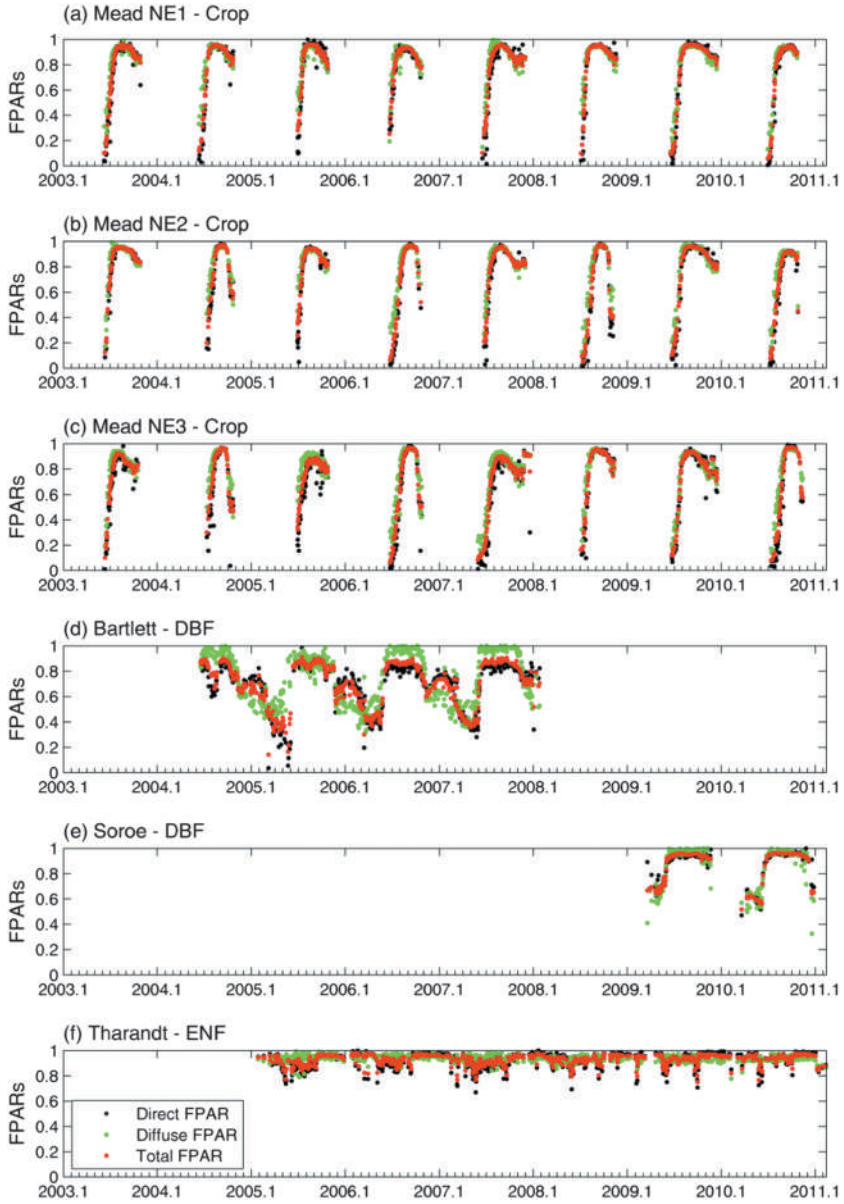

Figure 4. Seasonal variation of field-measured direct FPAR, diffuse FPAR, and total FPAR at six sites, (a) Mead NE1, (b) Mead NE2, (c) Mead NE3, (d) Bartlett, (e) Soroe, and (f) Tharandt.

efficiently than the direct PAR. Moreover, the field measured total FPAR is systematically higher than the direct FPAR (1.38–3.14%). In contrast, the total FPAR is slightly lower than the diffuse FPAR (−4.99 to −1.13%). The field-measured direct FPAR corresponds well to the total FPAR over crops and DBF sites ($R^2 >= 0.85$). It should be noted that the FPARs at the crop and DBF sites include contributions from all parts of the canopy (green leaves, yellow leaves, stems, branches, and seeds), whereas the ENF FPARs correspond only to the top canopy layer (green leaves and branches) as the PAR sensor is 17 m above the ground (Table 1).

The relative differences between field-measured diffuse and direct FPARs vary across the season (Figure 5). For the crops sites, the diffuse FPAR is larger than the direct FPAR during the beginning and ending of the season, and reach a minimum in summer (Figure 5a). The average differences for crop sites before and after the senescence are 9.95% and −3.45%, respectively (Table 4a). For the Bartlett and Soroe sites, the diffuse FPAR is larger than the direct FPAR by 19.38% and 2.68%, respectively, from April to September, but smaller than the latter by −7.56% and −14.74%, respectively, in winter (Figure 5b and Table 4a). Conversely, for the

Table 3. The Linear Regression Relationship Between Field Measured FPAR Components[a]

	Crops				DBF				ENF			
	N	R^2	RMSE	Bias (Relative)	*N*	R^2	RMSE	Bias (Relative)	*N*	R^2	RMSE	Bias (Relative)
$FPAR_{dif}$ versus $FPAR_{dir}$	2169	0.82	0.14	0.06 (8.56%)	935	0.45	0.17	0.04 (5.75%)	1673	0.18	0.07	0.02 (2.53%)
$FPAR_{tol}$ versus $FPAR_{dir}$	2169	0.96	0.06	0.02 (3.14%)	935	0.85	0.08	0.01 (1.81%)	1673	0.67	0.04	0.01 (1.38%)
$FPAR_{tol}$ versus $FPAR_{dif}$	2169	0.91	0.09	−0.04 (−4.99%)	935	0.75	0.11	−0.03 (−3.73%)	1673	0.4	0.04	−0.01 (−1.13%)

[a]$FPAR_{dir}$, $FPAR_{dif}$, and $FPAR_{tol}$ correspond to direct FPAR, diffuse FPAR, and total FPAR, respectively. DBF and ENF represent deciduous broadleaf forest and evergreen needleleaf forest, respectively. *N* represents the number of data points.

ENF site, the seasonality of the differences between direct and diffuse FPARs is less clear than those of the crop and DBF sites (Figure 5c). The diffuse FPAR is slightly lower than the direct FPAR by −1.51% in winter, but higher in other months (2.27%).

The relative differences between field-measured total and direct FPARs also vary across the season (Figure 6). For the crops sites, the relative differences are larger during the early growing season but are close to zero in the peak growing season. The total FPAR is higher than the direct FPAR by 8.0% –14.39% before senescence, but slightly lower than the latter by around 1% after senescent stage. On the DBF sites, the relative differences are generally within ±10%, although there is some scatters in the data points (particularly in winter). The average difference is 4.65% from April to September, and −6.20% during the other months (Table 4b). For the ENF site, the relative differences between the total FPAR and direct FPARs remain constantly small (<1.0%) throughout the year (Table 4b).

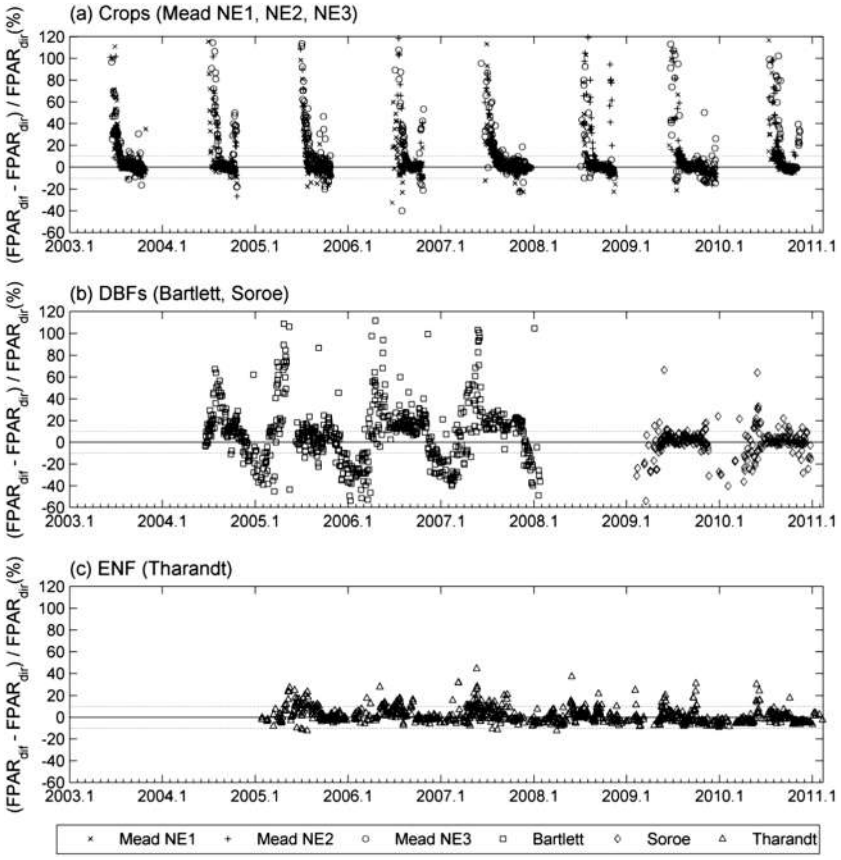

Figure 5. Seasonal variation of the relative difference between diffuse FPAR ($FPAR_{dif}$) and direct FPAR ($FPAR_{dir}$) from field measurements over (a) three crops sites including Mead NE1, NE2, and NE3 sites, (b) two DBF sites including Bartlett and Soroe sites, and (c) Tharandt site. DBF and ENF correspond to deciduous broadleaf forest and evergreen needleleaf forest, respectively. The dashed lines represent the ±10% relative differences.

Table 4a. $FPAR_{dif} - FPAR_{dir}$[a]

	Mead NE1	Mead NE2	Mead NE3	Bartlett	Soroe	Tharandt
Greenup to senescence	5.53%	11.14%	13.17%	19.38%	2.68%	2.27%
Other months	−4.87%	−5.05%	0.42%	−7.56%	−14.74%	−1.51%

[a]The relative difference between field measured diffuse FPAR ($FPAR_{dif}$) and direct FPAR ($FPAR_{dir}$) on five sites during the greenup to senescent stage and the other months. The greenup to senescent stages for crops and DBFs are May to September and April to September, respectively. For ENF site, only the nonwinter and winter (November to February) stages are separated.

3.3. The Landsat-Estimated FPARs

Figure 7 shows examples of direct, diffuse, and total FPARs estimated from Landsat during the summer season over three sites. On crops and DBF sites, the diffuse FPAR exhibits higher values and smaller spatial variation compared to the total FPAR (0.51–3.83%), whereas the direct FPAR is lower than the diffuse FPAR and total FPAR but exhibits a greater spatial variation (0.71–5.65%). On the Tharandt site, direct FPAR show slightly higher FPAR value than the diffuse and total FPAR, but with a smaller spatial variation (2.9%).

The Landsat-estimated diffuse FPAR corresponds very well to the direct FPAR over all sites ($R^2 > 0.98$) (Figure 8a). The diffuse FPAR is higher than the direct FPAR over the crops and DBFs sites by 0.87–2.95%, but slightly lower over the ENF site (−6.8%) (Table 5). The total FPAR has a very good relationship with the direct and diffuse FPAR ($R^2 > 0.99$). On crops and DBF sites, the total FPAR is slightly larger than the direct FPAR by 0.52–0.78%, but lower than the diffuse FPAR by −2.24–0.34%. Conversely, the total FPAR is smaller than the direct FPAR (−3.23%), whereas larger than the diffuse FPAR on the ENF site (3.84%).

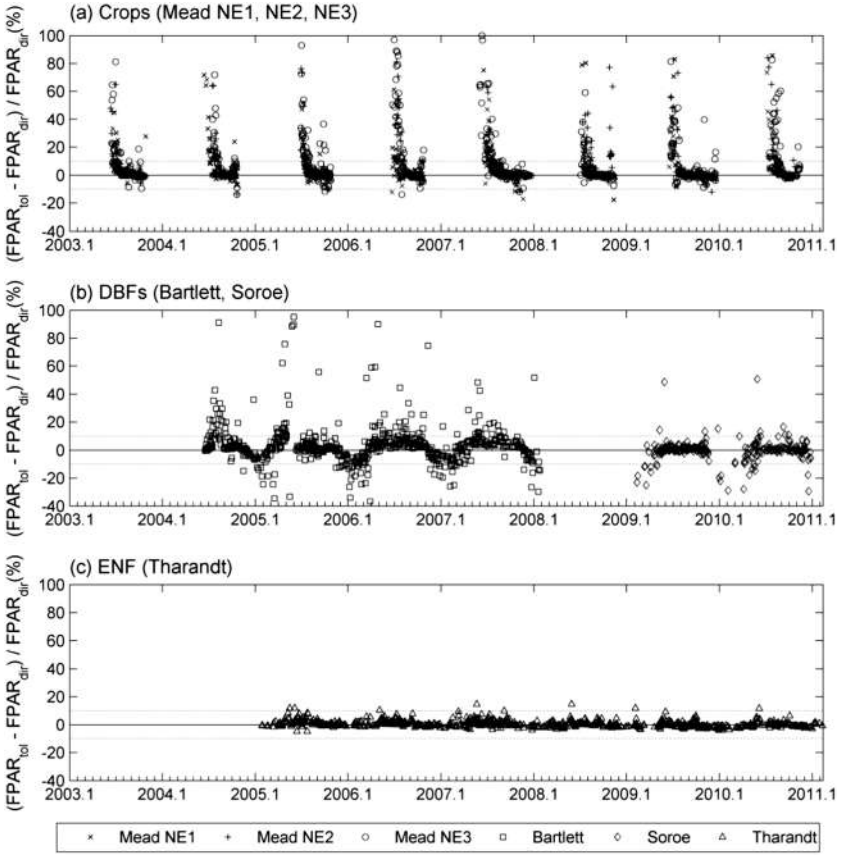

Figure 6. Seasonal variation of the relative difference between total FPAR ($FPAR_{tol}$) and direct FPAR ($FPAR_{dir}$) from field measurements over (a) three crops sites including Mead NE1, NE2, and NE3 sites, (b) two DBF sites including Bartlett and Soroe sites, and (c) Tharandt site. DBF and ENF correspond to deciduous broadleaf forest and evergreen needleleaf forest, respectively. The dashed lines represent the ±10% relative differences.

Table 4b. $FPAR_{tol} - FPAR_{dir}$ [a]

	Mead NE1	Mead NE2	Mead NE3	Bartlett	Soroe	Tharandt
Greenup to senescence	14.39%	16.07%	8.00%	7.87%	1.42%	0.64%
Other months	−1.37%	−1.55%	0.79%	−3.43%	−8.96%	−0.58%

[a]The relative difference between field measured total FPAR ($FPAR_{tol}$) and direct FPAR ($FPAR_{dir}$) on five sites from greenup to senescence and the other months. The greenup to senescent stages for crops and DBFs are May to September and April to September, respectively. For ENF site, only the nonwinter and winter (November to February) stages are separated.

Figure 9 compares the Landsat-estimated FPAR with corresponding field measurements. In general, all Landsat-estimated FPARs correspond well with the field measurements. The Landsat-estimated direct FPAR is slightly higher than the field measurements by 1.17%, whereas the Landsat diffuse FPAR is lower than the field measurements by −6.77%. Compared with the field-measured total FPAR, the Landsat total FPAR is larger by 1.64%, whereas the Landsat direct FPAR is slightly lower by 0.2%.

3.4. The Landsat-Estimated APARs

The differences between FPARs will influence the estimation of APARs. The direct and diffuse APARs were calculated using the field-measured direct and diffuse PAR, multiplied by the corresponding Landsat-estimated direct and diffuse FPARs (equations (2) and (3)) (Figure 10a). Generally, the relative difference between the direct and diffuse APAR decreases with increasing diffuse ratio ($R^2 = 0.76$), and the diffuse APAR tends to be lower than the direct APAR when diffuse ratio smaller than 50%. Conversely, the diffuse APAR is higher than the direct APAR when the diffuse ratio is larger than 50%. On average, the diffuse APAR is lower than the direct APAR by $-421.36\ \mu mol\ s^{-1}\ m^{-2}$ (−37.03%). The Landsat-estimated direct and total APARs were also calculated by multiplying the corresponding Landsat direct and total FPARs, respectively, by the field-measured downwelling

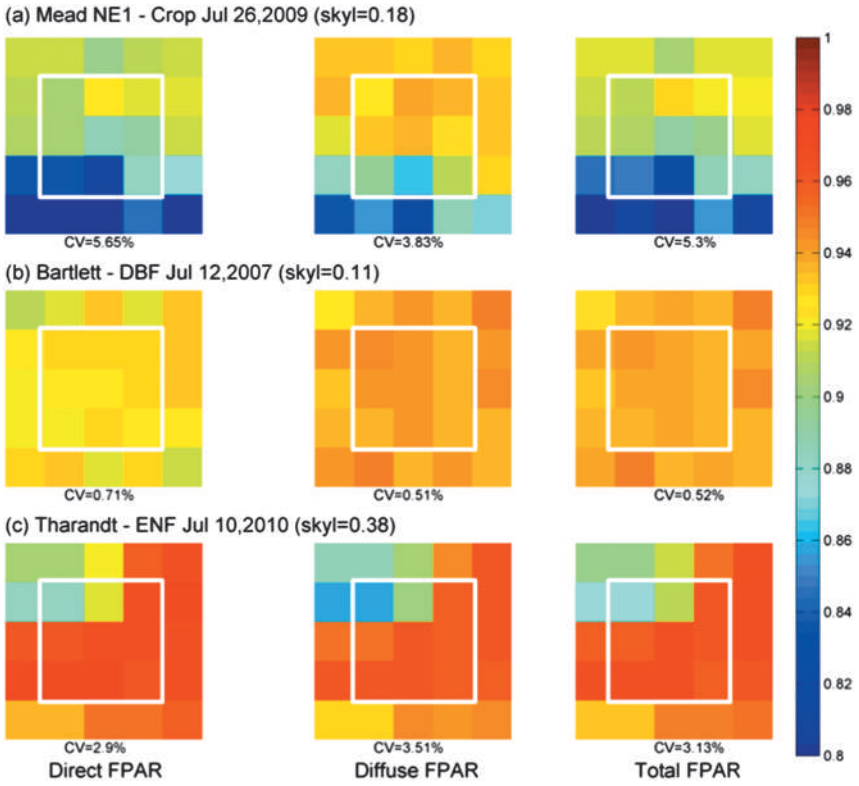

Figure 7. Landsat-estimated direct, diffuse, and total FPAR over three sites, (a) Mead NE1, (b) Bartlett, and (c) Tharandt. skyl represents the diffuse ratio measured in the field. DBF and ENF represent the deciduous broadleaf forest and the evergreen needleleaf forest, respectively. CV represents the coefficient of variation, which is calculated as the ratio of the standard deviation to the mean values. The white square represents the 3 × 3 pixel boarder.

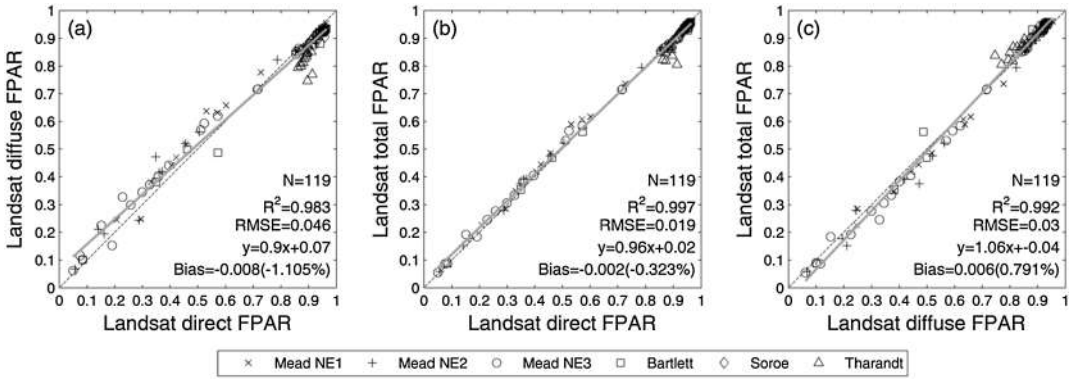

Figure 8. Comparison between Landsat-estimated FPAR components on six FLUXNET sites.

PAR. In general, the total APAR is higher than the direct APAR (277.72 μmol s^{-1} m^{-2}, 62.97%), and the difference increases with the diffuse ratio ($R^2 = 0.76$) (Figure 10b).

4. Discussion

4.1. Comparison of Direct and Diffuse FPARs

Both field and Landsat-estimated direct and diffuse FPARs demonstrate that green canopies have stronger absorption efficiency for diffuse PAR compared to direct PAR for crops, DBFs, and ENF. Our results are similar to those of other studies [*Nouvellon et al.,* 2000; *Thomas et al.,* 2006]. The separated direct and diffuse FPAR information is required in the gross primary production (GPP) calculation in a two-leaf light use efficiency model [*He et al.,* 2013]. Previous studies have also suggested that regional and global primary production models should consider the partition of direct and diffuse PAR [*Gu et al.,* 2002]. The direct and diffuse FPAR estimated in this study would help simulate canopy APAR, photosynthesis, and primary production for direct and diffuse PAR separately.

The relative difference between the direct and diffuse FPAR is mainly related to the canopy structure and the solar zenith angle. When LAI and solar zenith angle are small for crops and DBFs in the spring (Figures 3, 4a, and 4b), the diffuse FPAR is considerably higher than the direct FPAR (5.53–19.38%) because the evenly distributed diffuse radiation can be efficiently absorbed without obvious blocking from the upper layer. When LAI reaches the maximum, the diffuse FPAR is slightly smaller than or equal to the direct FPAR because the top green layer of the canopy absorb most of the direct and diffuse radiation and block the lower parts from the radiation FPAR. During the senescent stage, the decreasing LAI and increasing solar zenith angle lead to a stronger canopy absorption capacity for direct PAR. For the evergreen forests, the canopy structure remains stable during the whole year. The slight seasonal variation of the difference on the ENF site is mainly due to the changes of solar zenith angle. The large solar zenith angle in the winter (>70°) may have diminished the difference of canopy absorption for diffuse and direct FPARs. The nongreen elements of crops and DBFs in senescent stage and of ENF may also influence canopy absorption efficiency for direct and diffuse PARs.

Table 5. The Linear Regression Relationship Between Landsat-Estimated FPAR Components[a]

	Crops				DBF				ENF			
	N	R^2	RMSE	Bias (Relative)	*N*	R^2	RMSE	Bias (Relative)	*N*	R^2	RMSE	Bias (Relative)
$FPAR_{dif}$ versus $FPAR_{dir}$	82	0.988	0.04	0.01 (0.87%)	22	0.99	0.04	0.02 (2.95%)	15	0.17	0.07	−0.06 (−6.80%)
$FPAR_{tol}$ versus $FPAR_{dir}$	82	0.999	0.02	0.004 (0.52%)	22	0.99	0.01	0.01 (0.78%)	15	0.27	0.04	−0.03 (−3.23%)
$FPAR_{tol}$ versus $FPAR_{dif}$	82	0.994	0.03	−0.002 (−0.34%)	22	0.99	0.03	−0.02 (−2.24%)	15	0.75	0.04	0.03 (3.84%)

[a]$FPAR_{dir}$, $FPAR_{dif}$, and $FPAR_{tol}$ correspond to direct FPAR, diffuse FPAR, and total FPAR, respectively. DBF and ENF represent deciduous broadleaf forest and evergreen needleleaf forest, respectively. *N* represents the number of data points.

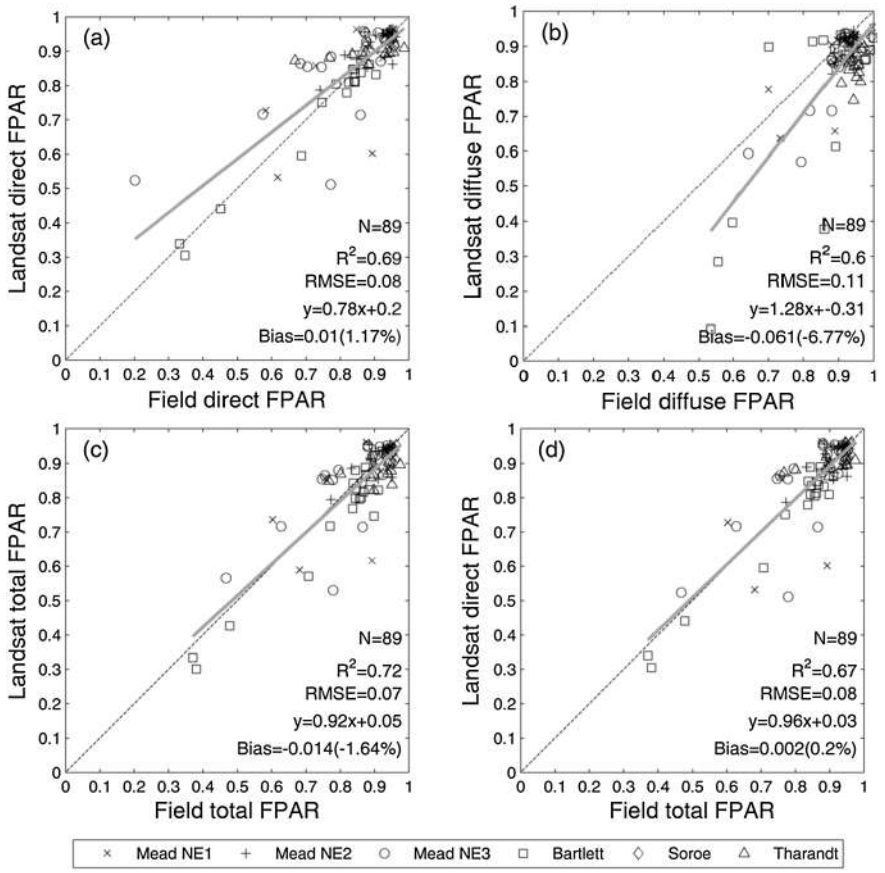

Figure 9. Validation of Landsat-5 estimated FPARs with field measured values. All field measurements are instantaneous values at 10:00 A.M.

The difference between the direct and diffuse APARs is closely related to the diffuse ratio (Figure 10a). This difference is also affected by the amount of the direct and diffuse PARs. In the present study, field-measured direct and diffuse PARs were used in the calculation of APAR. However, extension of the method to a large scale will be limited by the number of sites equipped with diffuse sensors. To date, several remote sensing PARs products have been generated [*Liang et al.,* 2013, 2006; *Zheng et al.,* 2008], but few of them provide direct and diffuse PARs separately. To better estimate canopy photosynthesis and primary production for direct and diffuse PAR separately, both PAR and FPAR may need to be partitioned.

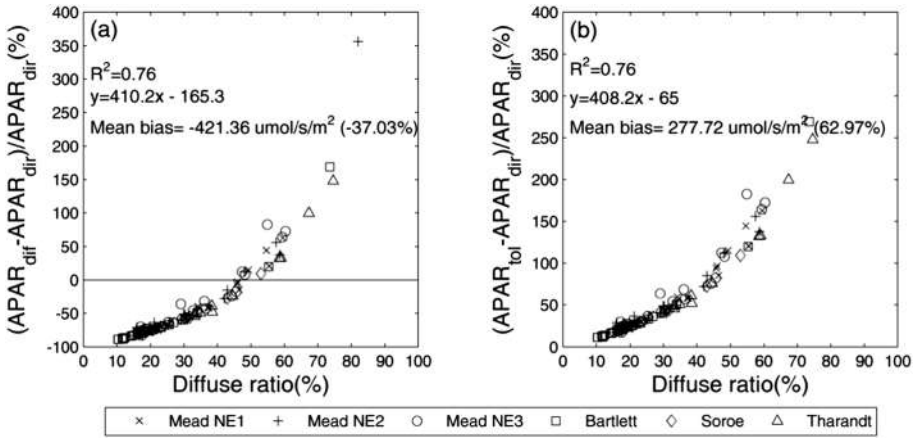

Figure 10. (a) The relative differences between diffuse APAR ($APAR_{dif}$) and direct APAR ($APAR_{dir}$) as a function of diffuse ratio. (b) The relative differences between total APAR ($APAR_{tol}$) and direct APAR ($APAR_{dir}$) as a function of diffuse ratio.

4.2. Comparison of Direct and Total FPARs

The direct FPAR is a function of canopy structure and Sun position but is not impacted by atmospheric conditions. Conversely, the diffuse FPAR is only influenced by the canopy structure. As the weighted sum of direct and diffuse FPAR, the total FPAR is influenced by the canopy structure, solar zenith angle, and the diffuse ratio. Our results from both satellite and field estimates indicate that the direct FPAR is lower than the total FPAR, especially for small LAI (Figure 5 and Table 4b). *Goward and Huemmrich* [1992] have demonstrated that the direct FPAR could underestimate the total FPAR by 10% for LAI < 2. Similar underestimation of the direct FPAR has also been reported by *Tian et al.* [2004]. Our results also show that the differences between direct and total FPARs are very small during the LAI peak stage (Figure 6 and Table 5), indicating that the direct FPAR may be used as a proxy of the total FPAR during this stage.

The direct usage of direct FPARs estimated by satellite in biogeochemical models may underestimate light absorption, gross primary production, and net primary production, especially for canopies with small LAI. The results show that the APAR calculated from direct FPAR is systematically smaller than that calculated from the total FPAR (on average 277.72 μmol s^{-1} m^{-2}). Even under the clear-sky conditions (skyl $< 20\%$), the direct APAR can underestimate the total APAR by up to 20.51% (Figure 10b). It has been reported that the standard MODIS GPP products, estimated from the MODIS black-sky FPAR, underestimate the ground values in tropical forests [*Propastin et al.,* 2012]. The MODIS GPP algorithm may also underestimate the field measurements under cloudy conditions because of the usage of the lower black-sky FPAR caused by the higher diffuse ratio [*Running and Zhao*, 2011]. However, this underestimation can be rectified by using the field-measured total FPAR [*He et al.,* 2010] or satellite-based total FPAR.

Many previous studies have validated the black-sky FPAR products using the field-measured total FPAR [*D'Odorico et al.,* 2014; *Fensholt et al.,* 2004; *Huemmrich et al.,* 2005; *Olofsson and Eklundh*, 2007], and underestimation of the black-sky FPARs has been reported for MODIS [*D'Odorico et al.,* 2014; *Olofsson and Eklundh*, 2007; *Senna et al.,* 2005], Spinning Enhanced Visible and Infrared Imager [*Martínez et al.,* 2013], and MERIS Global Vegetation Index [*D'Odorico et al.,* 2014; *Martínez et al.,* 2013]. These underestimations may be explained, to some degree, by the differences between the black-sky and total FPARs. To meet the requirements of the vegetation modeling community, the total FPAR can be generated in future from satellite data and validated with the corresponding field values.

4.3. Uncertainties and Prospects

The nongreen parts of the canopy will inevitably influence the comparison between field measurements and Landsat estimations. The field-measured FPAR through above and below-canopy PAR sensors includes contributions from the whole canopy, whereas the Landsat estimation only corresponds to the green FPAR. One green layer canopy was simulated and green FPARs were generated for crops. For forests, the brown bark influences the absorption throughout the year. A two-layer canopy consisting of one green and one brown layer was thus simulated using the SLC model. The generated FPARs are not strictly green FPAR but close to the field measurements in definition. Moreover, only images from greenup to senescent stages were selected. The good correspondence between the Landsat-estimated and field-measured FPAR values has shown the feasibility of our method. Indeed, more robust validation of the Landsat FPAR would require the separation of green parts from nongreen parts in field measurements.

The present study provides a means of estimating the direct and diffuse FPARs from the field measurements, by taking the total FPAR obtained with the largest diffuse ratio during a day as an approximation of the diffuse FPAR. The uncertainty of this approximation depends on the diffuse ratio error (compared with 1.0) and the difference between the direct and diffuse FPAR. In this study, the average maximum diffuse fractions (and the standard deviation) during the study period are 0.92 (0.12), 0.87 (0.08), 0.90 (0.1), 0.94 (0.05), 0.99 (0.02), and 0.84 (0.11) on the six sites, respectively (Figure 2). The errors for the diffuse ratio in the ENF site could be up to 16%. The uncertainties of estimated diffuse and direct FPARs could range from 0 (LAI > 3) to 15% (LAI $<= 3$). For other sites, the errors for the diffuse ratio are less than 10%, indicating the uncertainties in the estimated direct and diffuse FPARs may have an inherent error smaller than 10%. The estimated direct and diffuse FPARs can certainly be improved using a diffuse ratio of close to 1.0 when more frequent field PAR measurements (e.g., every minute) are available instead of the 30 min data used.

The Landsat-estimated direct and diffuse FPAR data set in this study can be used to validate the moderate-resolution FPAR products (e.g., black-sky FPAR from MODIS, GEOV1, and JRC-TIP; white-sky FPAR from JRC-TIP). The field-measured diffuse ratio, obtained concurrently with the satellite overpass, is crucial in estimating the total FPARs from the satellite. However, field data are usually limited by the sparse number of observations and clouds. For regional and global FPAR estimation, the diffuse ratio data may be obtained through satellite observations. The digital hemispheric photography provides a promising way to measure the direct and diffuse FPAR in the field [*Weiss and Baret,* 2010a, 2010b]. Separated estimations of PAR and FPAR for direct and diffuse components provide an opportunity to improve the estimation of canopy photosynthesis and primary production.

5. Conclusions

This paper developed a method to estimate the direct, diffuse, and total FPARs from Landsat 30 m surface reflectance data by using a canopy radiative transfer model and a lookup table inversion algorithm. Instantaneous direct and diffuse FPARs were estimated from field-measured FPAR over crops, deciduous broadleaf forests, and evergreen needleleaf forests. The differences between the direct and diffuse FPARs are mainly related to canopy structure and the solar zenith angle. The direct FPAR is generally lower than the total FPAR, and this difference increases for canopies with small LAI. The total FPAR should be generated from current satellite sensors, and the differences in FPAR definitions should be considered in the estimation of APAR in vegetation models. More frequent field measurements are necessary to improve the accuracy of ground FPAR measurements and to validate instantaneous satellite products. The present approach can be extended to estimate regional and global direct and diffuse FPAR products utilizing existing and future satellite data.

Acknowledgments

This study was supported by the Hundred Talent Program of the Chinese Academy of Sciences and the National Natural Science Foundation of China (41171333) (H. F.). We thank the FLUXNET network (http://public.ornl.gov/FLUXNET/), the site principal investigators, data collection and processing staff, and the agencies and institutions that funded long-term measurements at these sites. We thank the Landsat Surface Reflectance CDR project (http://landsat.usgs.gov/CDR_LSR.php) for providing long-term Landsat surface reflectance. The authors are thankful for the fruitful discussions with Frederic Baret and the comments from Shanshan Wei on an early version of the manuscript. We thank Wout Verhoef for the SLC software. We thank two anonymous reviewers and the Editors whose constructive comments help improved the manuscript.

References

Baret, F., et al. (2007), LAI, fAPAR and fCover CYCLOPES global products derived from VEGETATION Part 1: Principles of the algorithm, *Remote Sens. Environ.*, *110*, 275–286.

Baret, F., M. Weiss, R. Lacaze, F. Camacho, H. Makhmara, P. Pacholcyzk, and B. Smets (2013), GEOV1: LAI and FAPAR essential climate variables and FCOVER global time series capitalizing over existing products. Part1: Principles of development and production, *Remote Sens. Environ.*, *137*, 299–309.

Dai, Y., X. Zeng, R. E. Dickinson, I. Baker, and G. B. Bonan (2003), The Common Land Model (CLM) version 1.0, *Bull. Am. Meteorol. Soc.*, *84*, 1013–1023.

Darvishzadeh, R., A. Skidmore, M. Schlerf, and C. Atzberger (2008), Inversion of a radiative transfer model for estimating vegetation LAI and chlorophyll in a heterogeneous grassland, *Remote Sens. Environ.*, *112*, 2592–2604.

D'Odorico, P., A. Gonsamo, B. Pinty, N. Gobron, N. Coops, E. Mendez, and M. E. Schaepman (2014), Intercomparison of fractional absorbed photosynthetically active radiation products derived from satellite data over Europe, *Remote Sens. Environ.*, *142*, 141–154.

Fensholt, R., I. Sandholt, and M. S. Rasmussen (2004), Evaluation of MODIS LAI, fAPAR and the relation between fAPAR and NDVI in a semi-arid environment using in situ measurements, *Remote Sens. Environ.*, *91*, 490–507.

Foley, J. A., C. Prentice, N. Ramankutty, S. Levis, D. Pollard, S. Sitch, and A. Haxeltine (1996), An integrated biosphere model of land surface processes, terrestrial carbon balance, and vegetation dynamics, *Global Biogeochem. Cycles*, *10*, 603–628, doi:10.1029/96GB02692.

Ganguly, S., et al. (2012), Generating global Leaf Area Index from Landsat: Algorithm formulation and demonstration, *Remote Sens. Environ.*, *122*, 185–202.

GCOS (2011), Systematic observation requirements for satellite-based products for climate, 2011 update, supplemental details to the satellite-based component of the implementation plan for the Global Observing System for Climate in Support of the UNFCCC (2010 update), Reference Number GCOS-154, 138 pp. [Available at http://www.wmo.int/pages/prog/gcos/Publications/gcos-154.pdf.]

Gitelson, A. A., Y. Peng, J. G. Masek, D. C. Rundquist, S. Verma, A. Suyker, J. M. Baker, J. L. Hatfield, and T. Meyers (2012), Remote estimation of crop gross primary production with Landsat data, *Remote Sens. Environ.*, *121*, 404–414.

Gobron, N., and M. M. Verstraete (2009), Assessment of the status of the development of the standards for the terrestrial essential climate variables: Fraction of Absorbed Photosynthetically Active Radiation (FAPAR), Version 10, Version 10, 23 pp., Global Terrestrial Observing System, Rome. [Available at http://www.fao.org/gtos/doc/ECVs/T10/T10.pdf.]

Gobron, N., B. Pinty, M. Verstraete, and Y. Govaerts (1999), The MERIS Global Vegetation Index (MGVI): Description and preliminary application, *Int. J. Remote Sens.*, *20*(9), 1917–1927.

Gobron, N., et al. (2006), Evaluation of fraction of absorbed photosynthetically active radiation products for different canopy radiation transfer regimes: Methodology and results using Joint Research Center products derived from SeaWiFS against ground-based estimations, *J. Geophys. Res.*, *111*, D13110, doi:10.1029/2005JD006511.

Goward, S. N., and K. F. Huemmrich (1992), Vegetation canopy PAR absorptance and the normalized difference vegetation index: An assessment using the SAIL model, *Remote Sens. Environ.*, *39*, 119–140.

Grumwald, T., and C. Bernhofer (2007), A decade of carbon, water and energy flux measurements of an old spruce forest at the Anchor Station Tharandt, *Tellus*, *59B*, 387–396.

Gu, L., D. Baldocchi, S. B. Verma, T. A. Black, T. Vesala, E. M. Falge, and P. R. Dowty (2002), Advantages of diffuse radiation for terrestrial ecosystem productivity, *J. Geophys. Res.*, *107*(D6), 4050, doi:10.1029/2001JD001242.

He, M., Y. Zhou, G. Liu, W. Ju, X. Li, and G. Zhu (2010), Validation of MODIS gross primary productivity for a subtropical coniferous plantation in Southern China, in *Geoinformatics*, *2010 18th International Conference on June 18–20*.

He, M., et al. (2013), Development of a two-leaf light use efficiency model for improving the calculation of terrestrial gross primary productivity, *Agric. For. Meteorol.*, *173*, 28–39.

Houborg, R., M. Anderson, and C. Daughtry (2009), Utility of an image-based canopy reflectance modeling tool for remote estimation of LAI and leaf chlorophyll content at the field scale, *Remote Sens. Environ.*, *113*, 259–274.
Huemmrich, K. F., J. L. Privette, M. Mukelabai, R. B. Myneni, and Y. Knyazikhin (2005), Time-series validation of MODIS land biophysical products in a Kalahari woodland, Africa, *Int. J. Remote Sens.*, *26*, 4381–4398.
Jacquemoud, S., and F. Baret (1990), PROSPECT: A model of leaf optical properties spectra, *Remote Sens. Environ.*, *34*, 75–91.
Jenkins, J. P., A. D. Richardson, B. H. Braswell, S. V. Ollinger, D. Y. Hollinger, and M.-L. Smith (2007), Refining light-use efficiency calculations for a deciduous forest canopy using simultaneous tower-based carbon flux and radiometric measurements, *Agric. For. Meteorol.*, *143*, 64–79.
Knyazikhin, Y., J. V. Martonchik, R. B. Myneni, D. J. Diner, and S. W. Running (1998), Synergistic algorithm for estimating vegetation canopy leaf area index and fraction of absorbed photosynthetically active radiation from MODIS and MISR data, *J. Geophys. Res.*, *103*, 257–275, doi:10.1029/97JA02771.
Laurent, V. C. E., W. Verhoef, J. G. P. W. Clevers, and M. E. Schaepman (2011a), Estimating forest variables from top-of-atmosphere radiance satellite measurements using coupled radiative transfer models, *Remote Sens. Environ.*, *115*, 1043–1052.
Laurent, V. C. E., W. Verhoef, J. G. P. W. Clevers, and M. E. Schaepman (2011b), Inversion of a coupled canopy–atmosphere model using multi-angular top-of-atmosphere radiance data: A forest case study, *Remote Sens. Environ.*, *115*, 2603–2612.
Laurent, V. C. E., W. Verhoef, A. Damm, M. E. Schaepman, and J. G. P. W. Clevers (2013), A Bayesian object-based approach for estimating vegetation biophysical and biochemical variables from APEX at-sensor radiance data, *Remote Sens. Environ.*, *139*, 6–17.
Liang, S., T. Zheng, R. Liu, H. Fang, S.-C. Tsay, and S. Running (2006), Estimation of incident photosynthetically active radiation from Moderate Resolution Imaging Spectrometer data, *J. Geophys. Res.*, *111*, D15208, doi:10.1029/2005JD006730.
Liang, S., et al. (2013), A long-term Global LAnd Surface Satellite (GLASS) data-set for environmental studies, *Int. J. Digital Earth*, doi:10.1080/17538947.2013.805262.
Maiersperger, T. K., P. L. Scaramuzza, L. Leigh, S. Shrestha, K. P. Gallo, C. B. Jenkerson, and J. L. Dwyer (2013), Characterizing LEDAPS surface reflectance products by comparisons with AERONET, field spectrometer, and MODIS data, *Remote Sens. Environ.*, *136*, 1–13.
Martínez, B., F. Camacho, A. Verger, F. J. García-Haro, and M. A. Gilabert (2013), Intercomparison and quality assessment of MERIS, MODIS and SEVIRI FAPAR products over the Iberian Peninsula, *Int. J. Appl. Earth Obs. Geoinformation*, *21*, 463–476.
Masek, J. G., E. F. Vermote, N. E. Saleous, R. Wolfe, F. G. Hall, K. F. Huemmrich, F. Gao, J. Kutler, and T.-K. Lim (2006), A Landsat surface reflectance dataset for North America, 1990–2000, *IEEE Geosci. Remote Sens. Lett.*, *3*, 68–72.
Meroni, M., C. Atzberger, C. Vancutsem, N. Gobron, F. Baret, R. Lacaze, H. Eerens, and O. Leo (2013), Evaluation of agreement between space remote sensing SPOT-VEGETATION fAPAR time series, *IEEE Trans. Geosci. Remote Sens.*, *51*, 1951–1962.
Nouvellon, Y., A. Bégué, M. S. Moran, D. L. Seen, S. Rambal, D. Luquet, G. Chehbouni, and Y. Inoue (2000), PAR extinction in shortgrass ecosystems: Effects of clumping, sky conditions and soil albedo, *Agric. For. Meteorol.*, *105*, 21–41.
Ollinger, S. V., and M.-L. Smith (2005), Net primary production and canopy nitrogen in a temperate forest landscape: An analysis using imaging spectroscopy modeling and field data, *Ecosystem*, *8*, 760–778.
Olofsson, P., and L. Eklundh (2007), Estimation of absorbed PAR across Scandinavia from satellite measurements. Part II: Modeling and evaluating the fractional absorption, *Remote Sens. Environ.*, *110*, 240–251.
Pilegaard, K., P. Hummelshøj, N. O. Jensen, and Z. Chen (2001), Two years of continuous CO2 eddy-flux measurements over a Danish beech forest, *Agric. For. Meteorol.*, *107*, 29–41.
Pinty, B., I. Andredakis, M. Clerici, T. Kaminski, M. Taberner, M. M. Verstraete, N. Gobron, S. Plummer, and J. L. Widlowski (2011), Exploiting the MODIS albedos with the Two-stream Inversion Package (JRC-TIP): 1. Effective leaf area index, vegetation, and soil properties, *J. Geophys. Res.*, *116*, D09105, doi:10.1029/2010JD015372.
Propastin, P., A. Ibrom, A. Knohl, and S. Erasmi (2012), Effects of canopy photosynthesis saturation on the estimation of gross primary productivity from MODIS data in a tropical forest, *Remote Sens. Environ.*, *121*, 252–260.
Running, S., and M. Zhao (2011), Note to users on use of MODIS GPP/NPP (MOD17) datasets. [Available at https://lpdaac.usgs.gov/sites/default/files/public/about/docs/MOD17_NTSG_Note.pdf.]
Sellers, P. J. (1985), Canopy reflectance, photosynthesis and transpiration, *Int. J. Remote Sens.*, *6*, 1335–1372.
Senna, M. C. A., M. H. Costa, and Y. E. Shimabukuro (2005), Fraction of photosynthetically active radiation absorbed by Amazon tropical forest: A comparison of field measurements, modeling, and remote sensing, *J. Geophys. Res.*, *110*, G01008, doi:10.1029/2004JG000005.
Shuai, Y., J. G. Masek, F. Gao, and C. B. Schaaf (2011), An algorithm for the retrieval of 30-m snow-free albedo from Landsat surface reflectance and MODIS BRDF, *Remote Sens. Environ.*, *115*, 2204–2216.
Thomas, V., D. A. Finch, J. H. McCaughey, T. Noland, L. Rich, and P. Treitz (2006), Spatial modelling of the fraction of photosynthetically active radiation absorbed by a boreal mixedwood forest using a lidar-hyperspectral approach, *Agric. For. Meteorol.*, *140*, 287–307.
Tian, Y., et al. (2004), Comparison of seasonal and spatial variations of leaf area index and fraction of absorbed photosynthetically active radiation from Moderate Resolution Imaging Spectroradiometer (MODIS) and Common Land Model, *J. Geophys. Res.*, *109*, D01103, doi:10.1029/2003JD003777.
Verhoef, W. (1984), Light scattering by leaf layers with application to canopy reflectance modeling: The SAIL Model, *Remote Sens. Environ.*, *16*, 125–141.
Verhoef, W., and H. Bach (2003), Simulation of hyperspectral and directional radiance images using coupled biophysical and atmospheric radiative transfer models, *Remote Sens. Environ.*, *87*, 23–41.
Verhoef, W., and H. Bach (2007), Coupled soil–leaf-canopy and atmosphere radiative transfer modeling to simulate hyperspectral multi-angular surface reflectance and TOA radiance data, *Remote Sens. Environ.*, *109*, 166–182.
Verma, S. B., et al. (2005), Annual carbon dioxide exchange in irrigated and rainfed maize-based agroecosystems, *Agric. For. Meteorol.*, *131*, 77–96.
Weiss, M., and F. Baret (2010a), CAN-EYE V6.1 User Manual. [Available at http://www6.paca.inra.fr/can-eye/Documentation-Publications/Documentation.]
Weiss, M., and F. Baret (2010b), fAPAR (fraction of Absorbed Photosynthetically Active Radiation) estimates at various scale, *34th International Symposium on Remote Sensing of Environment*. [Available at http://www.isprs.org/proceedings/2011/ISRSE-34/211104015Final00926.pdf.]
Weiss, M., F. Baret, R. B. Myneni, A. Pragnère, and Y. Knyazikhin (2000), Investigation of a model inversion technique to estimate canopy biophysical variables from spectral and directional reflectance data, *Agronomie*, *20*, 3–22.
Zhang, Q., X. Xiao, B. Braswell, E. Linder, F. Baret, and B. Moore III (2005), Estimating light absorption by chlorophyll, leaf and canopy in a deciduous broadleaf forest using MODIS data and a radiative transfer model, *Remote Sens. Environ.*, *99*, 357–371.
Zheng, T., S. Liang, and K. Wang (2008), Estimation of incident photosynthetically active radiation from GOES visible imagery, *J. Appl. Meteorol. Climatol.*, *47*, 853–868.